Journal of Materials Chemistry C

ROYAL SOCIETY OF CHEMISTRY

PAPER

View Article Online
View Journal | View Issue

Cite this: J. Mater. Chem. C, 2022, 10, 9035

Tailoring the interface assembly of mesoporous TiO_2 on BTO film toward high-performance UV photodetectors†

Li Su,[ab] Ziqing Li,[c] Fa Cao,[ab] Xinya Liu[a] and Xiaosheng Fang *[a]

Received 15th April 2022,
Accepted 16th May 2022

DOI: 10.1039/d2tc01559e

rsc.li/materials-c

TiO_2-based nanomaterials are considered the most promising photoelectric materials for the construction of high-performance ultraviolet photodetectors. Nevertheless, they have always suffered from poor interface crystallinity that restricts the generation of photogenerated carriers and limits the enhancement of properties. Herein, a high-performance mesoporous titanium dioxide based ultraviolet photodetector fabricated on a self-polarized $BaTiO_3$ film (denoted as BTO@mTO) was introduced by an interface assembly strategy and spin-coating, through an in-situ annealing process. Due to the self-polarization of the ferroelectric phase $BaTiO_3$ and highly crystalline interface layer, the efficient separation of carriers is facilitated. Hence, the responsivity of BTO@mTO PD is up to 8.53×10^{-3} A W^{-1} under 310 nm. Compared with pure mTO PD, the I_{ph}/I_d ratio of BTO@mTO PD increased 17 times to 680.

1. Introduction

Even though ultraviolet (UV) radiation accounts only for less than 10% of the total solar radiation, it has huge effects on human health and life. Whether in military or civilian applications, UV detection shows great application values including missile early warning, secure space communication, anti-counterfeiting, and radiation curing.[1–3] Moreover, numerous studies have shown that ultraviolet radiation is a major cause of skin cancer.[4–6] Hence, ultraviolet photodetectors (UV PDs) have been extensively investigated for better monitoring and forewarning UV radiation. Presently, semiconductor-based UV PDs are one of the most widely studied monitoring devices, which are based on the photoconductive effect of semiconductor materials. Now, the wide band-gap semiconductors such as SiC and GaN have emerged as potential candidates for UV photodetection because of their high-strength chemical bonding structures and visible blindness.[7–9] However, the performance of this semiconductor-based UV photodetection is limited by the relatively low-quality oxide layer and high surface states/defects, which causes a slow recovery of the photocurrent. In addition, the fabrication process of semiconductors is usually harsh and complicated, thus hindering the practical applications of high-performance UV photodetection. Thanks to the excellent chemical inertness, low toxicity and photoconductivity properties of titanium dioxide, TiO_2-based UV PDs are one of the most promising, safe and reliable detectors. Generally, there are two routes to realize TiO_2-based UV PDs from the viewpoint of the device structure.[10,11] The problem of photogenerated carrier recombination often exists in early single TiO_2 UV PD, resulting in a slow response speed and low on/off ratio.[12–14] To promote the separation of photogenerated carriers, a p-n heterojunction of TiO_2 composite materials was developed.[15–17] For example, Xu and colleagues used the anodization process to construct a fiber-shaped UV PD of p-CuZnS/n-TiO_2, which shows high spectral responsivity at 0 bias.[6] Zheng *et al.* subsequently reported an inorganic-organic heterojunction (TiO_2/P3HT), which still needs to be modified with Au nanoparticles to further improve the responsivity and selectivity.[18] Despite this photodetector exhibiting self-powered characteristics, the stability and sensitivity remain a problem because of the limited warpage and the risk of surface photoelectric material shedding. Besides, a high-quality junction is often based on expensive and complicated fabrication processes, hindering the practical utilization. Therefore, how to develop a novel nanostructure involving TiO_2-based UV PD to effectively improve the photogeneration carrier efficiency through a facile strategy is still a challenge.

Previously, numerous studies have demonstrated that the unique photoelectric characteristics of functional mesoporous material are beneficial to the generation and the collection of charge carriers without quick charge recombination.[15,19–21] At present, research on functional mesoporous TiO_2 is mainly

[a] Department of Materials Science, Fudan University, Shanghai 200433, P. R. China. E-mail: xshfang@fudan.edu.cn
[b] Zhangjiang Fudan International Innovation Center, Shanghai 201210, P. R. China
[c] Institute of Optoelectronics, Fudan University, Shanghai 200433, P. R. China

† Electronic supplementary information (ESI) available. See DOI: https://doi.org/10.1039/d2tc01559e

focused on the design of photoelectric energy conversion. For instance, Giordano *et al.* demonstrated that Li-doped mesoporous TiO_2 electrodes in solar cells exhibit super electronic properties, which can reduce electronic trap states, enabling faster electron transport.[19] Zhao's group reported high photoelectric conversion efficiency dye-sensitized solar cells based on uniform 3D mesoporous TiO_2 microspheres, which benefit from the single-crystalline-like anatase walls that dominate (101) exposed facets.[20] The results suggested that highly crystalline TiO_2-based mesoporous materials show promising applications in high-performance photovoltaic devices such as solar cells. A few studies showed that the UV photodetector consisted of a mesoporous TiO_2 layer and a p-type organic layer (Spiro-OMeTAD) to form a dipole field, which affects the charge transfer and then the photocurrent/photoresponse.[21] However, mesoporous photoelectric detection is still rarely reported. This may be mainly due to the characteristics of the photoelectric detection principle, which converts UV radiation signals to electronic signals according to the photoelectric effect. On the one hand, the response time and conductivity of a film-type UV PD are greatly influenced by the depletion layer formed.[22–24] The depletion layer can be regulated by the built-in electric field of ferroelectric materials.[25] A stable in-built electric field introduced by the intrinsic self-polarization of ferroelectric film can effectively separate photogenerated carriers, which is expected to have potential applications in optoelectronic or photovoltaic fields.[26–28] Due to the excellent self-polarization characteristics, the inorganic ferroelectric barium titanate ($BaTiO_3$, BTO) appears naturally in ferroelectrics to adjust and optimize the system electron concentration without electrodes and external electric field.[29,30] For instance, Zhang *et al.* presented a single ZnO-based film UV PD with an enhanced on/off ratio (up to 14 300) due to the polarization of the ferroelectric $BaTiO_3$ film.[31] Moreover, the highly crystalline optoelectronic material is another key point for high-performance UV PD. For mesoporous materials, the surface characteristics of the substrate play a key role in controlling the mesoporous arrangement and crystallinity.[32,33] Qin *et al.* utilized ultrathin $BaTiO_3$ as a buffer layer to modify the mesoporous TiO_2 layer, which controlled the carrier separation efficiency.[30] Hence, the $BaTiO_3$ film with ferroelectricity is a good substrate for fabricating high-quality mesoporous TiO_2 film.

Herein, we have elaborately designed and fabricated a heterojunction film consisting of $BaTiO_3$@mesoporous TiO_2 (denoted as BTO@mTO) by an interface assembly strategy, spin-coating, and in-situ annealing process. The BTO@mTO UV PD demonstrates high responsivity (8.53×10^{-3} A W^{-1}) and excellent spectral selectivity under 310 nm light illumination. This profits from the regular mesoporous structure of TiO_2 and excellent interfacial crystallization between the TiO_2 layer and $BaTiO_3$ layer. The first-principles calculations of structure optimization and system energy convergence show that $BaTiO_3$ is used as a buffer layer to improve the crystallization of the mesoporous TiO_2 film. Moreover, the hysteresis loop result confirmed the ferroelectricity of $BaTiO_3$, which generated a built-in electric field by self-polarization to promote the separation of photogenerated carriers.

2. Experimental procedure

2.1 Synthesis of BTO film

The uniform thin tetragonal barium titanate ($BaTiO_3$ denoted as BTO) film was synthesized according to the sol-gel method reported in an early literature method.[31] With slight modifications, 0.038 mol acetic acid was added to PVP isopropyl solution (PVP = 0.08 g, M_w = 5500, C = 0.01 g mL^{-1}). Subsequently, 0.0057 mol titanium isopropoxide was added dropwise to the above solution with constant stirring for 1 h. Meanwhile, barium acetate (according to the stoichiometric ratio: Ba : Ti = 1 : 1) was dissolved in deionized water to form a transparent solution that was added dropwise to the titanium precursor solution, followed by stirring for 1 h. The obtained BTO sol was spin-coated on quartz substrates (ultrasonic cleaning of quartz plate with ethanol and acetone) at a speed of 3000 rpm for 30 s and immediately heated on 300 °C hot plate for 15 min. The BTO gel film was further crystallized by annealing at 700 °C for 2 h at a rate of 2 °C min^{-1} in air.

2.2 Synthesis of mesoporous TiO_2 precursor solution

Based on the typical sol-gel preparation method, 0.014 mol HCl and 6.7×10^{-5} mol H_2SO_4 were added dropwise into 10 mL ethanol under continuous stirring until uniformly dispersed, and 0.3 g F127 (or 0.3 g P123) was further added to the above solution at 40 °C for 3 h in an oil bath. Subsequently, 0.0034 mol titanium isopropoxide was slowly added to the above solution, which was heated and stirred for 12 h. The non-mesoporous titanium dioxide (denoted as TO) precursor solution had no pore-forming agent in the synthesis steps.

2.3 Interface assembly of mesoporous TiO_2 film on BTO film

The fabrication strategy of solvent evaporation induced self-assembly at the liquid-solid interface, the prepared TiO_2 precursor solution was spin-coated on the surface of BTO film at a speed of 2500 rpm for 30 s, and the obtained film was annealed at 450 °C for 2 h at a rate of 2 °C min^{-1} in air. The heterojunction film was obtained by mesoporous TiO_2 assembly at the $BaTiO_3$ film surface after annealing and natural cooling.

2.4 Instrumentation

X-Ray diffraction (XRD) was carried out on a Bruker D8-A25 diffractometer with Cu Kα radiation (λ = 1.5405 Å). The morphologies and microstructures of the as-prepared BTO@mTO were characterized by field-emission scanning electron microscopy (SEM) images recorded using a Zeiss Sigma microscope operating at 5 kV. A dual-beam FIB microscope Strata 400S (FEI) was used to prepare and test the BTO@mTO film (Si as a substrate). A Pt protection layer was deposited on the exposed target surface, which was FIB ablated at 30 kV into a prism-shape (10 μm length × 3 μm width × 5 μm depth). Further, the sample was mounted onto a Cu TEM grid and milled down to an 80 nm thin lamella. The TEM and HRTEM images were recorded by a Talos F200s transmission electron microscope operated at 200 kV. The film thicknesses were analyzed by AFM using a Bruker Dimension Edge instrument. The optical absorption spectra of the films were analyzed using

a UV-vis spectrophotometer with an integrating sphere attachment (Hitachi U-3900H). The temperature-dependent fluorescence spectra at 180 K were measured using an Edinburgh FLS980. The nanoporous structures of mTO film were analyzed by nitrogen sorption isotherms at 78 K using the Micromeritics ASAP 2460 Version 3.01. The specific surface areas were calculated by the Brunauer–Emmett–Teller (BET) method using adsorption. The Barrett–Joyner–Halenda (BJH) model was used to capture the pore size distribution from the adsorption branch. The ferroelectric properties of the BTO film (Hysteresis loop curve) were determined by using a BKT-2600 at an alternating current frequency of 100 Hz and an amplitude of −/+1 V with 2 cm^2 electrode area and test thickness of 200 nm at 22 °C.

2.5 Photoelectric measurements

The same area size of silver paste was spot-coated on the film surface as electrodes. All the electric and photoelectric measurements of the as-prepared devices were collected using a semiconductor characterization system (Keithley 4200, USA) connected to a 75 W Xe lamp as the light source and monochromator. A NOVA power meter (OPHIR photonics) was used to detect the light density. A YAG:Nb laser (pulse duration: 3–5 ns, 355 nm, Continuum Electro-Optics, Minilite II) with a 1 GΩ resistor and an oscilloscope (Tektronix MSO/DPO5000) was also used.

3. Results and discussion

The barium titanate composite mesoporous titanium dioxide heterojunction thin film ($BaTiO_3$@mesoporous TiO_2, denoted as BTO@mTO) was fabricated by the interface assembly strategy and the subsequent annealing crystallization process as described in Fig. 1a. The barium titanate precursor solution was spin-coated on a plasma cleaning quartz substrate to form a gel film, which was subsequently annealed at a high temperature to remove the surfactant and improve the BTO film crystallization quality. The solvent evaporation-induced self-assembly (EISA) is a representative liquid-solid interfacial assembly route that has been used for the fabrication of various mesoporous materials, such as mesoporous thin films.[32] The mesoporous titanium dioxide precursor solution was further spin-coated on the BTO film surface. It was carried out by a cooperative interface assembly of soft templates and framework precursors. With the evaporation of the solvent, the low molecular weight titanium precursor molecules further condensed and co-assembled with the soft-template molecules (F127, PEO-PPO-PEO), resulting in the formation of the mesostructured as-made gel film. After the dynamic assembly step, the solidification of mesostructures and elimination of the templates can be accomplished by calcination, and combined with a framework transformation, and a targeted mesoporous architecture can be produced.

The characteristic structure and crystalline phase information of BTO@mTO and the corresponding pure phase powders (after the volatilization of the solution in precursor, the obtained TiO_2 gel and $BaTiO_3$ gel were annealed under the same condition) were analyzed by X-ray diffraction (XRD) patterns (Fig. 1b). The $BaTiO_3$ film and the powder have the same characteristic diffraction peaks located at 31.6°, 38.9°, 45.4° and 56.3°, which correspond to the tetragonal phase barium titanate (110), (111), (201) and (211) crystal planes (JCPDS No. 05-0626).[28] Moreover, the characteristic diffraction peaks of the pure phase TiO_2 powder are in agreement with anatase titanium dioxide (JCPDS No. 21-1272).[18] It is worth noting that only one diffraction peak of BTO@mTO film located at 25.3° was assigned to the (101) plane of anatase titanium dioxide, while indistinct signals for barium titanate were observed. The one reason may be that the mTO film was compactly coated on the BTO film surface, leading to the corresponding $BaTiO_3$ characteristic peak signal being difficult to collect. The other may be attributed to the film having orientation characteristics, which weakened the characteristic diffraction peak intensity. The speed of mesostructure formation of TO film was too fast in the non-aqueous system (namely, volatilization completed instantaneously), resulting in the varied shrinkage of the solid-liquid interface that caused the uneven size of micelles or channels, which led to the broadening of diffraction peaks. According to the Scherrer formula, the peak widths at half maximum (FWHM) and corresponding particle sizes of titanium dioxide for both BTO@mTO film and powder were 0.827, 0.634 and 1.701, 2.216 (Fig. 1c). Compared with the powder, the film has finer grains, which improves the interface crystallinity. Subsequently, Raman spectroscopy was conducted to verify the presence of anatase in the BTO@mTO film. Fig. S1a (ESI†) shows the characteristic peaks at 141 cm^{-1} and 638 cm^{-1} due to the O–Ti–O symmetric E_g anatase vibration mode, which confirmed the anatase phase of TiO_2, consistent with the XRD results.[18,34]

The morphology and mesostructure of mTO film were characterized by scanning electron microscopy (SEM). A flat surface with a uniform and clear mesoporous structure was observed, which exhibited a short-range ordered hexagonal arrangement and average pore size of about 11 nm (Fig. 1d). The porous structure of the mTO film was further determined by the nitrogen sorption technique (Fig. 1e). It displayed a type-IV isotherm with a surface area of 207 $m^2\ g^{-1}$ calculated by the Brunauer–Emmett–Teller (BET) model, and steeper adsorption at the condensation section indicated a relatively uniform distribution of the pore size. Moreover, it shows a typical H2 hysteresis loop at a relative pressure P/P_0 of 0.4–0.7, demonstrating that the mTO film has typical spherical pores with narrow pore windows.[35–37] Hence, compared with the open mesopores on the mTO surface, the mesopore size distribution with an average diameter of the film was only 5.5 nm as estimated by the Barrett-Joyner-Halenda (BJH) method (Fig. S1b, ESI†). The transmission electron microscopy (TEM) image of mTO showed that the mesopore size ranged from 6 nm to 9 nm, which is consistent with the BJH results (Fig. S1c, ESI†). To gain more insight into the interface structure of BTO@mTO film, the cross-sectional SEM images and corresponding surface morphology SEM images are illustrated in Fig. 1f and g. The cross-sectional SEM images show that the BTO film with 194 nm thickness was uniformly and densely deposited on the substrate surfaces, and the dense and smooth

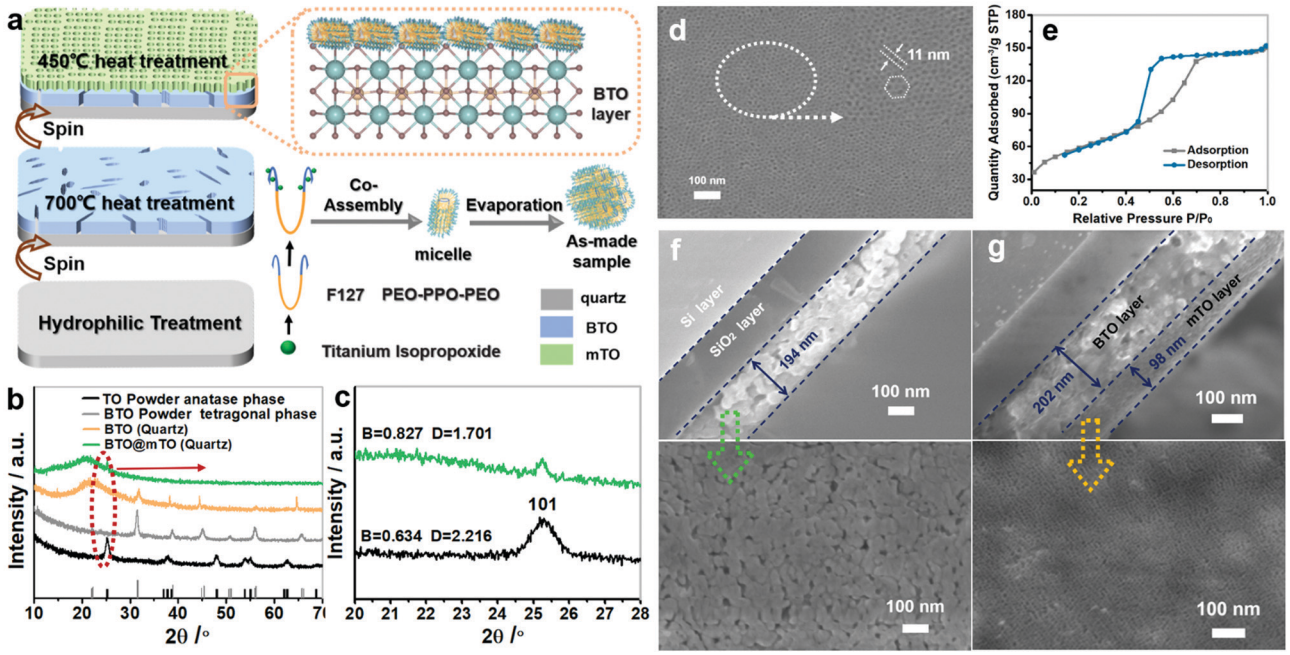

Fig. 1 (a) Schematic of the preparation process of BTO@mTO thin film. (b) and (c) XRD patterns of films and the corresponding pure powders, and the enlargement image of the characteristic diffraction peak of the (101) plane in anatase. (d) and (e) SEM image and nitrogen adsorption-desorption isotherms of mTO film (a certain mass of mTO powder scraped from the substrate was collected for the nitrogen adsorption and desorption tests, which avoided the error caused by the substrate). (f) and (g) The cross-sectional SEM images and the corresponding surface SEM images of BTO film and BTO@mTO film (based on the electron microscopy test condition, and Si wafer with SiO_2 thin layer as the substrate).

surface of the film consisted of nanoscale crystal grains. The BTO film can provide a promising platform for interfacial assembly to integrate various devices. Therefore, the interfacial assembly of micelles on the BTO film surface to fabricate the mesoporous framework in which BTO and mTO are staggered to form a well-interacting interface after annealing will benefit the photoelectric properties. The cross-sectional SEM image of the BTO@mTO film displays the uniform and smooth interface between the BTO layer and mTO layer, which have thicknesses of 202 nm and 98 nm, respectively. Particularly, mTO shows a smooth surface and maintains a uniform mesoporous structure, while it has poor ordering. The electrical and photodetection properties of both mTO and BTO@mTO photodetectors with Ag electrode (denoted as mTO PD and BTO@mTO PD) were systematically investigated by a two-probe method under monochromatic illumination. The current–voltage (*I*–*V*) curve of mTO PD in a logarithmic plot under dark and 320 nm light illumination, which fielded a low dark current of 0.04 pA and a photocurrent of 0.47 μA at 3.0 V bias (Fig. 2a) showed that the mTO film exhibited good photoelectric detection performance.

To further investigate the influence of microstructure on the photoelectric properties, titanium dioxide films with different morphologies were fabricated by adjusting the pore-forming conditions and characterized. The TiO_2 PDs were obtained based on the triblock copolymer P123 and non-pore-forming agent (denoted as mTO-P123 PDs and TO PDs, respectively). As shown in the SEM image, the mTO-P123 film presents a clear and flat surface with a uniform mesoporous structure and has poor order (Fig. S2a, ESI†). The lower hydrophilic-hydrophobic ratio led to the decrease in the anisotropy of P123 in non-aqueous systems. Hence, the triblock copolymer F127 with a higher hydrophilic-hydrophobic ratio is more suitable as a soft template to form a highly ordered mesoporous structure. Compared with the mesoporous structure, the TO film showed a smooth and compact surface without an obvious mesoporous structure (Fig. S2b, ESI†). The subsequent photoelectric test based on *I*–*V* curves showed that mTO-P123 PD also yielded a low dark current of 0.06 pA and a photocurrent of 17.7 pA at 3 V bias voltage, which was significantly lower than mTO (Fig. S2a, ESI†). For TO PD, the dark current and photocurrent were 6.6 pA and 1.04 nA at 3 V bias voltage, respectively (Fig. S2b, ESI†). Using UV-vis absorption spectra, the optical properties of the films were characterized for better insight into the correlation between microstructure and properties. It was observed that all three titanium dioxide films showed a negligible absorption over the visible range and a sharp absorption edge at 320 nm, with which the optical bandgap was estimated by the Tauc plots (Fig. S3a and b, ESI†). Although the titanium dioxide films have substantially the same optical bandgap, the mTO film showed stronger absorption intensity. This indicates that the film with a highly ordered mesoporous structure can absorb more ultraviolet light, which provides the potential for transparent and high-performance UV-responsive devices.

Subsequently, the photoelectric performance of BTO@mTO PD was investigated (Fig. 2b and c). Different incident wavelengths were compared, and the *I*–*V* curves of BTO@mTO PD showed that the photocurrent was up to 3.94 μA and a dark current of 25 pA under 320 nm at 3 V. Moreover, the

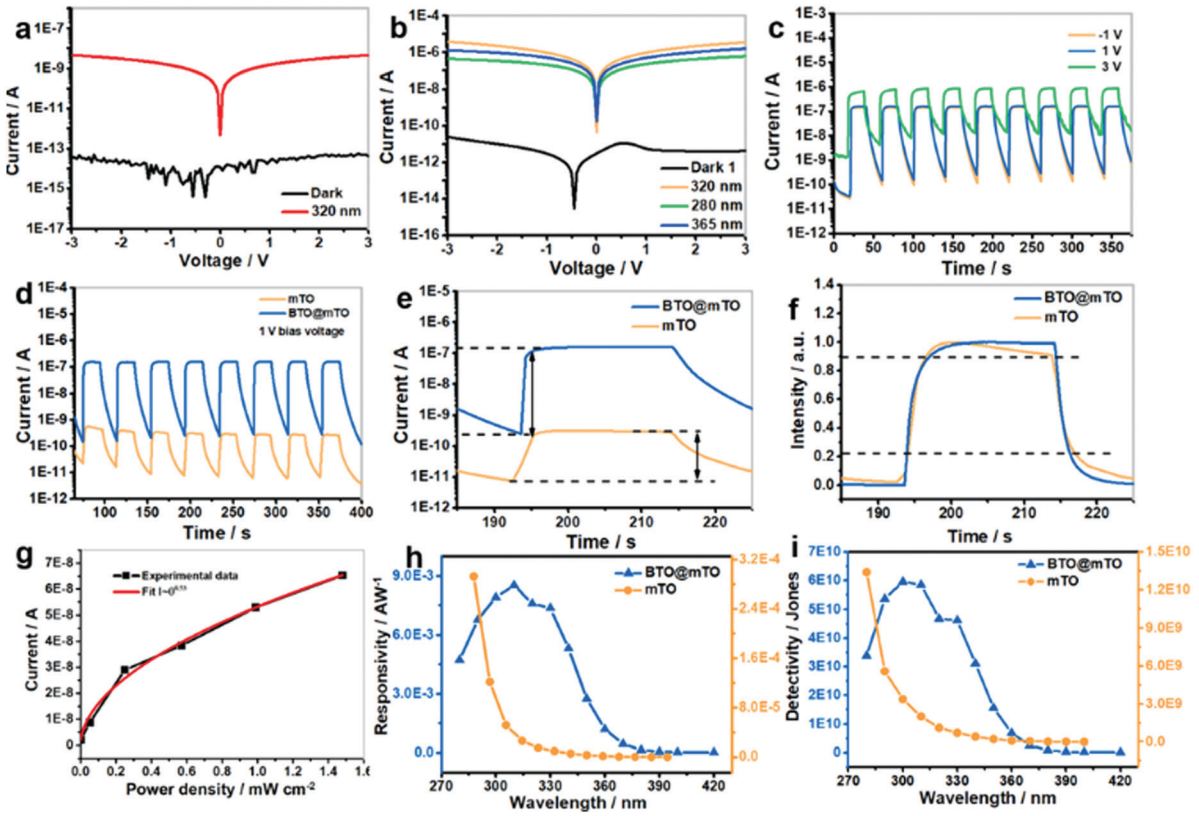

Fig. 2 (a) The semi-logarithmic *I*–*V* curves of the mTO film under 320 nm UV wavelength. (b) BTO@mTO film under different UV wavelengths. (c) *I*–*t* curves of BTO@mTO film under 320 nm UV on/off switching at various biases. (d) *I*–*t* characteristics under dark conditions and 320 nm UV wavelength at 1 V bias. (e) and (f) The single period of the *I*–*t* curves and the normalized *I*–*t* curves. (g) Experimental and fitted photocurrents as a function of the power density of the BTO@mTO UV sensor. (h) and (i) The responsivity and corresponding detectivity of mTO and BTO@mTO film.

time-resolved current (*I*–*t*) characteristics of BTO@mTO PD showed reproducibility without noticeable photocurrent decay at different biases and yielded a stable photocurrent of 0.16 μA at 1 V bias. In contrast, the periodical on/off UV light illumination photocurrent of mTO only increased to 0.37 pA at 1 V (Fig. 2d). Furthermore, the response time and photosensitivity, which can be defined as the ratio of photocurrent to dark current I_{ph}/I_d, were the key parameters that demonstrated the performance of the UV photoelectronic device. Fig. 2e illustrates a single period of the *I*–*t* curve on a semilogarithmic plot upon 320 nm UV irradiation to evaluate the on/off ratio of mTO PD and BTO@mTO PD. It was observed that the photocurrent of mTO decayed slowly from 0.3 nA to 7.5 pA in 20 s, resulting in a low I_{ph}/I_d ratio of 40. Due to the pronounced increase in the photocurrent, the I_{ph}/I_d ratio of the BTO@mTO increased to 680, which was 17 times higher than that of mTO PD. Besides, the time-dependent current curves were normalized to compare the response time, which is defined by the peak photocurrent rising from 10% to 90% and the peak photocurrent decaying from 90% to 10% (Fig. 2f). The results showed that the two PDs have very close rise times with 2.6 s for mTO and 3 s for BTO@mTO, respectively. mTO has a slower decay time (7.1 s) than BTO@mTO (3.2 s). The pulse response performance was characterized by a pulsed laser source for investigating the response time of BTO@mTO PD. It was estimated that the rise time and decay time were 0.74 ms and 65 ms, respectively, suggesting an outstanding response speed (Fig. S4, ESI†). On comparing different power densities, the photosensitivity of BTO@mTO PD further proved the positive effect of the BTO layer on the transport properties of photogenerated charge carriers. The results showed that the photocurrent steadily increases with respect to the increasing light intensity, which gives photocurrent values of 1.9 nA at 74.8 μW cm^{-2}, 11 nA at 283 μW cm^{-2}, 39 nA at 618 μW cm^{-2}, 42 nA at 1058 μW cm^{-2}, 53 nA at 1520 μW cm^{-2} and 66 nA at 2020 μW cm^{-2}, all at 1 V under 320 nm UV light illumination (Fig. S5, ESI†). The results showed that the photogenerated charge carrier efficiency is proportional to the absorbed photon flux. Moreover, the corresponding nonlinear relationship for the photocurrent variation against illuminance intensity can be fitted by the power-law relationship: $I_p = A_p\theta$, where *A* is a constant for wavelength, p refers to the irradiation intensity and the response of the photocurrent to irradiation intensity is determined by the exponent ($0.5 < \theta < 1$).[38] The calculated value of the non-unity exponent of the fitting curve is 0.53, suggesting a rather complex process including the generation, separation, recombination, and trapping of photogenerated charge carriers (electron–hole pairs) in BTO@mTO PD.[39–41] The spectral responses of both mTO PD and BTO@mTO PD were further investigated by varying the incident wavelength and can be calculated by spectral

responsivity ($R\lambda$) and specific detectivity (D^*), which are the crucial figures of merit for performance evaluation, where I_p and I_d are the photocurrent and dark current, $P\lambda$ and S are the incident power density and the effective irradiated area, e and λ are the Planck's constant and the wavelength, respectively.[42,43]

$$R\lambda = (I_p - I_d)/P\lambda \times S \quad (1)$$

$$D^* = R\lambda \times (2eI_d/S)^{-1/2} \quad (2)$$

Fig. 2h and i present the spectral responsivity of mTO PD and BTO@mTO PD from 280 nm to 420 nm at 1 V. The spectral responsivity of mTO PD decreased with the increase of incident wavelength, which reached the maximum value of 2.9×10^{-4} A W^{-1} under 280 nm. Moreover, the spectral responsivity of BTO@mTO PD first increased and then decreased with the increase of the incident wavelength. It has the optimum spectral responsivity of 8.53×10^{-3} A W^{-1} under 310 nm, and low spectral responsivity of the incident wavelength above 390 nm. The results show excellent spectral responsivity performance and UV light selective response characteristics. The detectivity (D^*) value is another important parameter that reflects the ability of the device to detect weak light signals from the noise environment. The detectivity of BTO@mTO PD achieved 5.8×10^{10} Jones, which exceeded the mTO PD.

The I–V curves of the BTO film showed that there was an insignificant photocurrent response under UV irradiation at 320 nm, proving that BTO has no ultraviolet photoelectric detection ability, therefore, the mTO film is the major photoelectric conversion material in BTO@mTO PD (Fig. S6, ESI†). In order to explore the effect of thickness for photoelectric detection performance, the mTO with different thickness by adjusting the spin-coating speed was further explored. The characterization was based on the atomic force microscopy (AFM) method; the BTO@mTO-1 film with 252.2 nm thickness was obtained at 3000 rpm, while BTO@mTO-2 with 229.5 nm thickness was obtained at 1250 rpm, which may be caused by the uneven glue (the film thickness includes the BTO layer, which was prepared in the same batch, and thus the error caused by the thickness of the BTO layer can be ignored) (Fig. S7b and c, ESI†). In contrast, the BTO@mTO film prepared at 2500 rpm had a thickness of 316.1 nm. This suggested that a too-fast or too-slow spin-coating speed will cause uneven glueing, thus reducing the thickness (Fig. S7a, ESI†). Subsequently, the I–V curves of BTO@mTO-1 PD and BTO@mTO-2 PD yielded a low dark current of 0.1 pA and 0.2 pA and the corresponding photocurrent reached 86 nA and 22 nA under 320 nm, respectively (Fig. S7d and e, ESI†). Fig. S8a and b (ESI†) display the I–t curves of BTO@mTO-1 PD and BTO@mTO-2 PD at various bias voltages, which show an on/off ratio of 10^3 at 1 V. Compared with BTO@mTO-1 PD and BTO@mTO-2 PD, BTO@mTO has a similar switching ratio and a higher photocurrent detection, suggesting that the thickness of the mTO film is positively related to the photodetection performance. Moreover, the BTO@mTO also showed superior responsivity and detectivity as compared with the reported TiO_2-based UV photodetectors (Table S1, ESI†).

Generally, the contact interface with high crystallinity is the key point affecting the transport and separation of photogenerated carriers. Hence, the contacting interface of BTO and mTO was characterized by focused ion beam (FIB) to display the original crystal structure. The cross-sectional TEM image indicated that the contacting interface was composed of the BTO layer of ~195 nm and mTO layer of 92 nm, consistent with SEM results (Fig. 3a). Moreover, the amorphous SiO_2 layer was produced by the oxidation of silicon atoms, which was proved by mapping images. High-resolution transmission electron microscopy (HR-TEM) displayed the interplanar spacings of 4.02 Å and 3.45 Å, corresponding to the tetragonal barium titanate (001) and (101) crystal planes (denoted as $BaTiO_3$(001) and $BaTiO_3$ (101)). The crystal lattice fringe around $BaTiO_3$ (101) was 2.9 Å, which belongs to the anatase titanium dioxide (101) crystal planes (denoted as TiO_2 (101)). The potential lattice match with the initial contact interface between $BaTiO_3$ (101) and TiO_2(101) was confirmed by first-principles structure optimization using CASTEP (Fig. 3b and c).[5] The Ti–O bonds were formed between the $BaTiO_3$ (101) outermost Ti atom and the starting point O atom of TiO_2 (101) to achieve the lowest energy and highest geometry optimization. The 2D unit cell of $BaTiO_3$ (101) is extremely close to that of TiO_2 (101) in shape and size, promoting an epitaxial-like growth of titanium dioxide on the barium titanate surface for forming a highly crystalline quality film, which is favorable for carrier transport (Fig. 4a). The BTO layer was used as a buffer layer to provide an excellent substrate for the interfacial assembly of the mTO film,

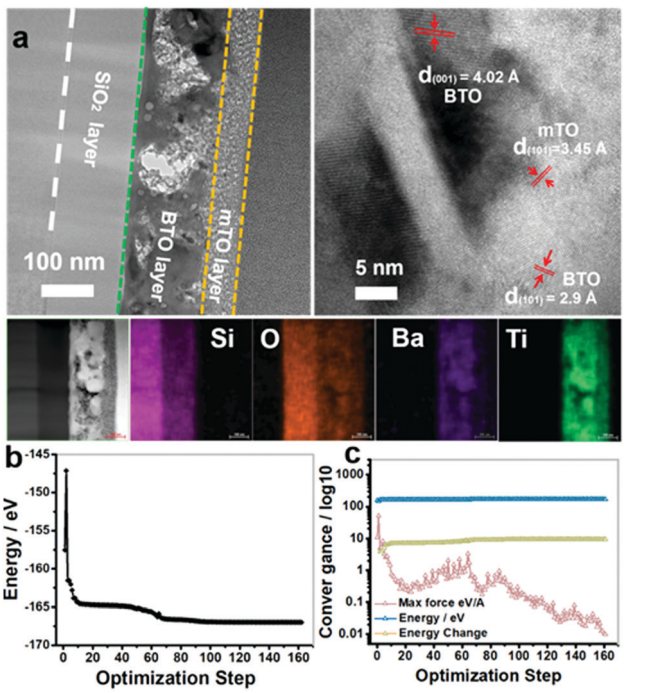

Fig. 3 (a) High-resolution TEM image of the cross-section of the interface between BTO@mTO and the Si wafer (SiO_2 thin layer derived from the Si wafer oxidized surface) and the corresponding element mapping images. (b and c) The energy minimization and geometry optimization during the optimization process by first principles.

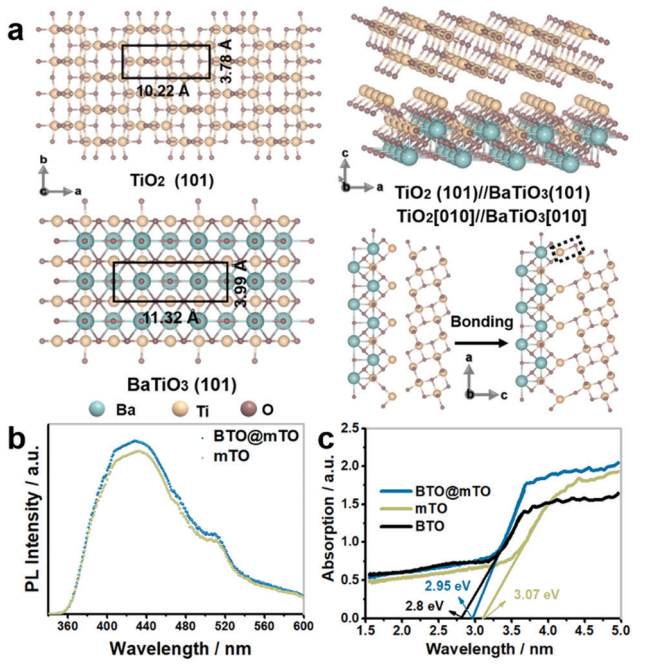

Fig. 4 (a) First-principles structure optimization started with anatase TiO_2 (101)-tetragonal $BaTiO_3$ (101). (b) The low-temperature fluorescence emission spectra with an excitation wavelength of 325 nm. (c) The Tauc curve from the corresponding UV-vis absorption spectra of mTO and BTO and BTO@mTO films.

improving the contact interface crystallinity. The low-temperature photoluminescence (PL) spectra at 180 K further confirmed this result. The broadening of fluorescence peaks under the excitation of 325 nm excitation light indicated that the films have a complex recombination process, which includes interband excitation behavior and defect recombination (Fig. S9, ESI†). The preliminary research on anatase showed that fluorescence originates from the radiative recombination of self-trapped excitons (STEs), which is attributed to the spontaneous self-localization of photogenerated charges occurring in polar semiconductors with strong electron–phonon coupling.[44,45] For anatase titanium dioxide, longer Ti–Ti interionic distances, lower TiO_6 octahedral coordination, and poorer symmetry are the prominent structural characteristics, which are beneficial for STE formation (based on the Toyozawa theory of self-localization).[46] By the fitted peaks from 400 nm to 450 nm, the intensity followed the interband excitation behavior, which competed with the relaxation and/or radiative recombination of the photogenerated electrons, suggesting that the conduction band (CB) electrons e_{CB}^- were responsible for this emission band.[47,48] The PL intensity of the BTO@mTO film was higher as compared to the mTO film, implying that the low surface defect density resulted from few grain boundaries (Fig. 4b). Moreover, the optical band-gap structures of both BTO@mTO film and mTO film were analyzed by UV-vis absorption spectroscopy and the corresponding Tauc curves (Fig. 4c and Fig. S3b, ESI†). The optical band-gap of the BTO@mTO film under the influence of the barium titanate layer was 2.95 eV narrower than that of the mTO film, and the absorption edge shifted to the long-wavelength direction. For the anatase phase, the UV light absorption (<400 nm) was mainly from the valence band (VB) to the conduction band (CB), that is, the electronic transition from O 2p to Ti 3d.

The polarization hysteresis (*P–E*) loop of the BTO buffer layer was measured at 100 Hz. It showed the ferroelectricity of barium titanate film but it did not reach saturation due to the electrical breakdown at higher voltages (Fig. 5a).[49–51] The surface

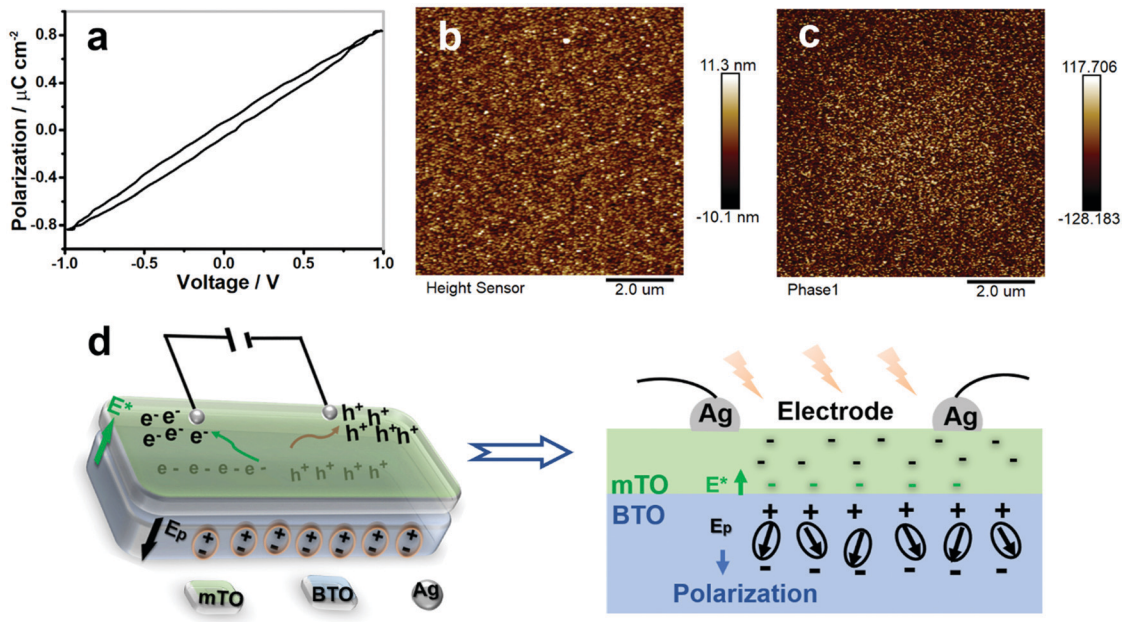

Fig. 5 (a) The hysteresis curve of the BTO ferroelectric film. PFM images of the BTO film: (b and c) height sensor image and phase image. (d) Schematic diagram of the built-in field formed by the self-polarization orientation and corresponding transport mechanism of photogenerated carriers in the interface between mTO and BTO.

morphologies and phase of BTO buffer layer were further obtained simultaneously under PFM mode. The height sensor results showed a smooth surface, as well as fine and uniform grains, indicating that the surface had good roughness, which is beneficial for the subsequent interface assembly of titanium dioxide (Fig. 5b). Besides, the out-of-plane domains were represented for the BTO layer, which indicated that the downward domain and the upward domain are shown by the dark brown regions and light brown regions (Fig. 5c). It can be clearly seen that the upward domains were fewer than the downward domains, indicating that a built-in electric field with a downward direction was formed by ferroelectric self-polarization in the BTO layer. The photoelectric transmission mechanism of the BTO@mTO PD provided more insight (Fig. 5d) into the unique mesoporous structure and the excellent interface crystallization quality, which all benefited the generation and transmission of the photogenerated carriers. The downward built-in electric field in the barium titanate can further promote the separation of carriers and the utilization of the carriers, achieving the purpose of improving the photoelectric performance.

4. Conclusions

In summary, the high-performance BTO@mTO UV PD was fabricated by an interface assembly strategy and simple spin-coating method. The good crystallinity of the interface between the $BaTiO_3$ film and TiO_2 film promoted the generation of photogenerated carriers, and the self-polarized electric field of $BaTiO_3$ regulated the separation of carriers. The BTO@mTO film device demonstrated a spectral responsivity of 8.53×10^{-3} A W^{-1} under 310 nm, and the I_{ph}/I_d ratio of BTO@mTO PD increased to 680, which is 17 times higher than pure mTO PD. The strategy of mesoporous structure interfacial assembly and employing self-polarized ferroelectric materials might provide a facile way to fabricate high-performance UV PD.

Conflicts of interest

There are no conflicts to declare.

Acknowledgements

The authors are grateful for financial support from National Natural Science Foundation of China (No. 12061131009 and 51872050), China Postdoctoral Science Foundation (2021M690647), the young scientist project of MOE innovation platform, and Science and Technology Commission of Shanghai Municipality (No. 21520712600 and 19520744300).

Notes and references

1 S. Kim, Y. T. Lim, E. G. Soltesz, A. M. De Grand, J. Lee, A. Nakayama, J. A. Parker, T. Mihaljevic, R. G. Laurence, D. M. Dor, L. H. Cohn, M. G. Bawendi and J. V. Frangioni, *Nat. Biotechnol.*, 2004, **22**, 93–97.
2 Y. H. Chen, L. X. Su, M. M. Jiang and X. S. Fang, *J. Mater. Sci. Technol.*, 2022, **105**, 259–265.
3 Y. Q. Bie, Z. M. Liao, H.-Z. Zhang, G. R. Li, Y. Ye, Y. B. Zhou, J. Xu, Z. X. Qin, L. Dai and D. P. Yu, *Adv. Mater.*, 2011, **23**, 649–653.
4 Z. Li, M. K. Joshi, J. Chen, Z. Zhang, Z. Li and X. S. Fang, *Adv. Funct. Mater.*, 2020, **30**, 2005291.
5 W. Yang, K. Hu, F. Teng, J. Weng, Y. Zhang and X. S. Fang, *Nano Lett.*, 2018, **18**, 4697–4703.
6 X. Xu, J. Chen, S. Cai, Z. Long, Y. Zhang, L. Su, S. He, C. Tang, P. Liu, H. Peng and X. S. Fang, *Adv. Mater.*, 2018, **30**, 1803165.
7 M. Spies, M. Hertog, P. Hille, J. Schörmann, J. Polaczynski, B. Gayral, M. Eickhoff, E. Monroy and J. Lahnemann, *Nano Lett.*, 2017, **17**, 4231–4239.
8 X. Wan, Y. Xu, H. W. Guo, K. Shehzad, A. Ali, Y. Liu, J. Y. Yang, D. X. Dai, C. T. Lin, L. W. Liu, H. C. Cheng, F. Q. Wang, X. M. Wang, H. Lu, W. D. Hu, X. D. Pi, Y. P. Dan, J. K. Luo, T. Hasan, X. F. Duan, X. M. Li, J. B. Xu, D. R. Yang, T. L. Ren and B. Yu, *npj 2D Mater. Appl.*, 2017, **1**, 4.
9 T. Journot, V. Bouchiat, B. Gayral, J. Dijon and B. Hyot, *ACS Appl. Mater. Interfaces*, 2018, **10**, 18857–18862.
10 F. Cao, L. Meng, M. Wang, W. Tian and L. Li, *Adv. Mater.*, 2019, **31**, 1806725.
11 L. Huang, J. Yang, X. Wang, J. Han, H. Han and C. Li, *Phys. Chem. Chem. Phys.*, 2013, **15**, 553–560.
12 X. Li, C. Gao, H. Duan, B. Lu, X. Pan and E. Xie, *Nano Energy*, 2012, **1**, 640–645.
13 Z. Wang, S. Ran, B. Liu, D. Chen and G. Shen, *Nanoscale*, 2012, **4**, 3350–3358.
14 Y. Xie, L. Wei, Q. Li, Y. Chen, H. Liu, S. Yan, J. Jiao, G. Liu and L. Mei, *Nanoscale*, 2014, **6**, 9116–9121.
15 Z. Li, Z. Li, C. Zuo and X. S. Fang, *Adv. Mater.*, 2022, **34**, 2109083.
16 L. Zheng, F. Teng, X. Ye, H. Zheng and X. S. Fang, *Adv. Energy Mater.*, 2020, **10**, 1902355.
17 W. Ouyang, F. Teng, J.-H. He and X. S. Fang, *Adv. Funct. Mater.*, 2019, **29**, 1807672.
18 L. Zheng, X. Deng, Y. Wang, J. Chen, X. S. Fang, L. Wang, X. Shi and H. Zheng, *Adv. Funct. Mater.*, 2020, **30**, 2001604.
19 F. Giordano, A. Abate, J. P. Correa Baena, M. Saliba, T. Matsui, S. H. Im, S. M. Zakeeruddin, M. K. Nazeeruddin, A. Hagfeldt and M. Graetzel, *Nat. Commun.*, 2016, **7**, 10379.
20 Y. Liu, R. Che, G. Chen, J. Fan, Z. Sun, Z. Wu, M. Wang, B. Li, J. Wei, Y. Wei, G. Wang, G. Guan, A. A. Elzatahry, A. A. Bagabas, A. M. Al-Enizi, Y. Deng, H. Peng and D. Zhao, *Sci. Adv.*, 2015, **1**, e1500166.
21 T. Zhu, J. Su, J. Alvarez, G. Lefèvre, F. Labat, I. Ciofini and T. Pauporté, *Adv. Funct. Mater.*, 2019, **29**, 1903981.
22 J. Zeng, X. Li, Y. Wu, D. Yang, Z. Sun, Z. Song, H. Wang and H. Zeng, *Adv. Funct. Mater.*, 2018, **28**, 1804394.
23 J. R.-D. Retamal, C.-Y. Chen, D.-H. Lien, M. R.-S. Huang, C.-A. Lin, C.-P. Liu and J.-H. He, *ACS Photonics*, 2014, **1**, 354–359.
24 G. Li, L. Meng, X. Zhu, W. Gao, Y. Qin and L. Chen, *Nanoscale*, 2018, **10**, 2242–2248.
25 Y. Zhang, W. Jie, P. Chen, W. Liu and J. Hao, *Adv. Mater.*, 2018, **30**, 1707007.

26 R. Guo, L. Shen, H. Wang, Z. Lim, W. Lu, P. Yang, Ariando, A. Gruverman, T. Venkatesan, Y. P. Feng and J. Chen, *Adv. Mater. Interfaces*, 2016, **3**, 1600737.
27 H. Lee, T. H. Kim, J. J. Patzner, H. Lu, J.-W. Lee, H. Zhou, W. Chang, M. K. Mahanthappa, E. Y. Tsymbal, A. Gruverman and C.-B. Eom, *Nano Lett.*, 2016, **16**, 2400–2406.
28 A. Gruverman, D. Wu, H. Lu, Y. Wang, H. W. Jang, C. M. Folkman, M. Y. Zhuravlev, D. Felker, M. Rzchowski, C. B. Eom and E. Y. Tsymbal, *Nano Lett.*, 2009, **9**, 3539–3543.
29 H. Lu, C.-W. Bark, D. E.-D. L. Ojos, J. Alcala, C. B. Eom, G. Catalan and A. Gruverman, *Science*, 2012, **336**, 59–61.
30 J. Qin, Z. Zhang, W. Shi, Y. Liu, H. Gao and Y. Mao, *ACS Appl. Mater. Interfaces*, 2018, **10**, 36067–36074.
31 Y. Zhang, X. Zhao, J. Chen, S. Li, W. Yang and X. S. Fang, *Adv. Funct. Mater.*, 2020, **30**, 1907650.
32 L. Duan, C. Wang, W. Zhang, B. Ma, Y. Deng, W. Li and D. Zhao, *Chem. Rev.*, 2021, **121**, 14349–14429.
33 C.-W. Wu, T. Ohsuna, M. Kuwabara and K. Kuroda, *J. Am. Chem. Soc.*, 2006, **128**, 4544–4545.
34 L. Zheng, S. Han, H. Liu, P. Yu and X. S. Fang, *Small*, 2016, **12**, 1527–1536.
35 H. Xu, J. Wu, W. Luo, Q. Li, W. Zhang and J. Yang, *Small*, 2020, **16**, 2001775.
36 Z. Zhang, C. Wang, G. Huang, H. Liu, S. Yang and A. Zhang, *J. Hazard. Mater.*, 2018, **357**, 73–80.
37 G.-H. Wang, Z. Cao, D. Gu, N. Pfänder, A.-C. Swertz, B. Spliethoff, H.-J. Bongard, C. Weidenthaler, W. Schmidt, R. Rinaldi and F. Schüth, *Angew. Chem., Int. Ed.*, 2016, **55**, 8850–8855.
38 Q. Hong, Y. Cao, J. Xu, H. Lu, J. He and J.-L. Sun, *ACS Appl. Mater. Interfaces*, 2014, **6**, 20887–20894.
39 H. Fang, C. Zheng, L. Wu, Y. Li, J. Cai, M. Hu, X. S. Fang, R. Ma, Q. Wang and H. Wang, *Adv. Funct. Mater.*, 2019, **29**, 1809013.
40 P. Yu, K. Hu, H. Chen, L. Zheng and X. S. Fang, *Adv. Funct. Mater.*, 2017, **27**, 1703166.
41 H.-Y. Chen, K.-W. Liu, X. Chen, Z.-Z. Zhang, M.-M. Fan, M.-M. Jiang, X.-H. Xie, H.-F. Zhao and D.-Z. Shen, *J. Mater. Chem. C*, 2014, **2**, 9689–9694.
42 H. Liu, Z. Zhang, L. Hu, N. Gao, L. Sang, M. Liao, R. Ma, F. Xu and X. S. Fang, *Adv. Opt. Mater.*, 2014, **2**, 771–778.
43 S. Li, Y. Zhang, W. Yang, H. Liu and X. S. Fang, *Adv. Mater.*, 2020, **32**, 1905443.
44 W. Ouyang, F. Teng and X. S. Fang, *Adv. Funct. Mater.*, 2018, **28**, 1707178.
45 H. Tang, H. Berger, P. E. Schmid, F. Lévy and G. Burri, *Solid State Commun.*, 1993, **87**, 847–850.
46 D. K. Pallotti, L. Passoni, P. Maddalena, F. Di Fonzo and S. Lettieri, *J. Phys. Chem. C*, 2017, **121**, 9011–9021.
47 Y. Toyozawa, *J. Lumin.*, 1981, **24-25**, 23–30.
48 A. Setaro, S. Lettieri, P. Maddalena and L. D. Stefano, *Appl. Phys. Lett.*, 2007, **91**, 051921.
49 S. Lettieri, M. Causà, A. Setaro, F. Trani, V. Barone, D. Ninno and P. Maddalena, *J. Chem. Phys.*, 2008, **129**, 244710.
50 J. P. George, J. Beeckman, W. Woestenborghs, P. F. Smet, W. Bogaerts and K. Neyts, *Nanoscale Res. Lett.*, 2013, **8**, 62.
51 Y. Feng, C. Wang, S. Tian, Y. Zhou, C. Ge, H. Guo, M. He, K. Jin and G. Yang, *Sci. China Phys. Mech.*, 2017, **60**, 067711.